Stellar Velocities in the Carina, Fornax, Sculptor and Sextans dSph Galaxies: Data from the Magellan/MMFS Survey[1]

Matthew G. Walker[1,2], Mario Mateo[2] and Edward W. Olszewski[3]

walker@ast.cam.ac.uk

ABSTRACT

We present spectroscopic data for individual stars observed from 2004 March through 2008 August as part of our Michigan/MIKE Fiber System (MMFS) survey of four dwarf spheroidal (dSph) galaxies: Carina, Fornax, Sculptor and Sextans. Using MMFS at the Magellan/Clay Telescope at Las Campanas Observatory, we have acquired 8855 spectra from 7103 red giant candidates in these Galactic satellites. We list measurements of each star's line-of-sight velocity (median error ± 2.1 km s^{-1}) and spectral line indices for iron and magnesium absorption features. We use globular cluster spectra to calibrate the indices onto standard [Fe/H] metallicity scales, but comparison of the resulting metallicities with published values suggests that the MMFS indices are best used as indicators of relative, not absolute metallicity. The empirical distributions of velocity and spectral indices also allow us to quantify the amount of contamination by foreground stars. In a companion paper we develop an algorithm that evaluates the membership probability for each star, showing that the present MMFS sample contains more than 5000 dSph members, including 774 Carina members, 2483 Fornax members, 1365 Sculptor members, and 441 Sextans members.

Subject headings: galaxies: dwarf — galaxies: kinematics and dynamics — (galaxies:) Local Group — galaxies: individual (Carina, Fornax, Sculptor, Sextans) — techniques: radial velocities

---

[1]Institute of Astronomy, University of Cambridge, UK

[2]Department of Astronomy, University of Michigan, Ann Arbor, MI

[3]Steward Observatory, The University of Arizona, Tucson, AZ

[1]This paper presents data gathered with the 6.5-m Magellan Telescopes at Las Campanas Observatory, Chile.

1. Introduction

Dwarf spheroidal (dSph) galaxies are the smallest stellar systems thought to contain dark matter. Because they represent the lower observational extreme of both the galaxy-luminosity and halo-mass functions, dSphs are important objects with which to compare models of galaxy formation. As dSphs typically lack neutral hydrogen, their pressure-supported stellar components provide the best available kinematic tracers. The dSph satellites of the Milky Way (MW) are sufficiently nearby that one can obtain high-resolution spectra of individual stars, enabling line-of-sight velocity measurements that resolve narrow (typically $\sim 5 - 10$ km s^{-1}) dSph velocity dispersions. The first such study used velocity measurements of just three stars to argue that the Draco dSph, if in virial equilibrium, has mass-to-light ratio $M/L \geq 30$ (solar units), indicative of a dominant dark matter component (Aaronson 1983).

Subsequent observations of Draco and other MW satellites supported the notion that dSph kinematics are dominated by dark matter. Stellar velocity samples containing measurements for tens of stars per galaxy showed that the most luminous dSphs ($L_V \sim 10^{5-7}L_{V,\odot}$) all have central velocity dispersions of ~ 10 km s^{-1} (e.g., Aaronson & Olszewski 1987; Mateo et al. 1991, 1993; Suntzeff et al. 1993; Hargreaves et al. 1994; Armandroff et al. 1995; Hargreaves et al. 1996; Olszewski et al. 1995; Queloz et al. 1995; Vogt et al. 1995; Mateo et al. 1998). Given such data, simple kinematic models that assume spherical symmetry, dynamic equilibrium, velocity isotropy and radially constant M/L (i.e., mass follows light) imply that dSphs have masses of $\sim 10^7$ M$_\odot$ and $M/L \sim 10^{1-2}$. The absence of a correlation between dynamical mass and luminosity suggests that the large variation in M/L is solely a reflection of the variation in baryon content (Mateo et al. 1993, 1998; Gilmore et al. 2007; Walker et al. 2007b; Strigari et al. 2008).

The advent of high-resolution, multi-object spectrographs at large telescopes now makes it possible to gather spectra for hundreds of stars during a single night. With samples reaching hundreds of stars per dSph, velocity dispersion profiles are now available for all of the brighter MW dSphs (Kleyna et al. 2002, 2004; Wilkinson et al. 2004; Muñoz et al. 2005, 2006; Sohn et al. 2007; Walker et al. 2006a,b, 2007b; Battaglia et al. 2006; Mateo et al. 2008; Koch et al. 2007b,a). For the most luminous dSphs it is now possible to build spectroscopic data sets for thousands of stars. With such large data sets one can measure higher moments (e.g., kurtosis) of the velocity distribution, and thereby place observational constraints on orbital anisotropy (Łokas et al. 2005). The large data sets also provide information about the velocity distribution in two dimensions and thus are capable of uncovering kinematic evidence of substructure (Kleyna et al. 2003; Walker et al. 2006b) as well as tidal streaming (Muñoz et al. 2006; Mateo et al. 2008). The ability to measure spectral line strengths from

these low S/N spectra provides an extra dimension of information that can be used to study stellar metallicity distributions (e.g., Koch et al. 2006, 2007b), to identify correlations between kinematics and metallicity (Tolstoy et al. 2004; Battaglia et al. 2006), and to help clean samples of contaminating foreground stars.

In a previous paper (Walker et al. 2007a, Paper I hereafter) we introduce a spectroscopic survey of individual dSph stars, undertaken using the Michigan/MIKE Fiber System (MMFS) at the Magellan 6.5-m Clay Telescope at Las Campanas Observatory. Our MMFS spectra have resolution $R \sim 20000$ and sample the region $5140 - 5180$ Å, which contains the prominent magnesium-triplet absorption feature. Paper I describes MMFS as well as our procedures for target selection, observation and data reduction. As of 2008 August we have used MMFS to obtain 8855 spectra from 7103 stars in four dSphs: Carina, Fornax, Sculptor and Sextans. From each spectrum we measure the line-of-sight velocity and spectral indices that quantify the strengths of the iron and magnesium absorption lines present in the spectra (Paper I).

Here we present the entire MMFS data set. In a companion paper (Walker et al. 2008, "Paper III" hereafter) we develop a statistical algorithm that uses the available velocity and magnesium data, as well as the stellar positions, to evaluate for each star the probability of dSph membership. Adding these probabilities, we find that the MMFS sample contains more than 5000 dSph members. In forthcoming papers we use the MMFS data to provide detailed analyses of dSph kinematics and chemodynamic substructure.

2. Observations & Data

We refer the reader to Paper I for a description of MMFS and the details of our methodology regarding target selection, observing procedure and data reduction. After the publication of Paper I we obtained new data during observing runs in 2007 January, 2007 September, 2008 April and 2008 August. In these runs we used MMFS to observe nine additional Carina fields (including five distinct sets of targets in the densely populated central field), three Sextans fields, eight Sculptor fields and six Fornax fields. Table 1 logs these new observations (see Paper I for a log of all previous MMFS observations). The first two columns identify the galaxy and field number (identified in the maps of Figure 1). Columns $3 - 7$ list the heliocentric Julian date at the midpoint of the first exposure, UT date at the midpoint of the first exposure, total exposure time, number of red giant candidates to which we assigned fibers, and the number of these for which we obtained an acceptable velocity measurement. The fraction of observed stars with acceptable measurements suffered in both 2007 runs due to harsh observing conditions. Figure 1 maps all dSph fields observed with MMFS as of 2008

August.

Tables 2, 3, 4 and 5 present the MMFS spectroscopic data from each individual observation of targets in Carina, Fornax, Sculptor and Sextans, respectively. For stars with multiple velocity measurements, results from repeat observations are listed directly beneath the first measurement. Otherwise, results are listed chronologically by time of observation. Column 1 identifies each target by galaxy and ID number. Column 2 gives the field number and spectrograph channel ("B" for blue, "R" for red) in which the star was observed. Column 3 lists the Heliocentric Julian Date of the observation. Columns $4-5$ list equatorial coordinates (J2000.0). Columns $6-7$ give the apparent V magnitude and $V-I$ color, respectively[2]. Column 8 lists the measured velocity in the heliocentric rest frame (HRF). Columns $9-10$ list composite spectral indices ΣFe and ΣMg, respectively.

We use repeat measurements of stars measured on both blue and red channels of the MIKE spectrograph to quantify any systematic difference that may arise due to channel-dependent dispersion characteristics (Bernstein et al. 2003; Paper I). For 647 stars we obtained at least one acceptable velocity measurement on both channels. For these stars, the left-hand panel of Figure 2 plots the velocity measured on the blue channel against that measured on the red channel. The best-fitting line through these data points has slope 0.998 ± 0.002 and intercept -0.33 ± 0.52 km s^{-1}, indicating there is no systematic difference between velocities measured with blue and red channels.

We find evidence for a slight channel-dependence in measuring magnesium strength. For 476 stars we obtained at least one acceptable measurement of ΣMg on both channels. For these stars, the right-hand panel in Figure 2 plots ΣMg$_{blue}$ against ΣMg$_{red}$. The best-fitting straight line is given by

$$\Sigma\text{Mg}_{blue} = (0.936 \pm 0.048)\Sigma\text{Mg}_{red} - (0.007 \pm 0.048)\text{Å}. \qquad (1)$$

For subsequent analysis we apply Equation 1 to place values of ΣMg measured with the red channel on the blue-channel scale. The values of ΣMg listed in Tables 2 - 5 for red-channel spectra are those obtained *after* applying Equation 1. We do not apply a similar correction, however, for values of ΣFe measured with the red channel, because red-channel values of ΣFe are calculated using fewer absorption lines than blue-channel values (the red channel has low throughput at the blue end of our spectral range; see Paper I). Blue- and red-channel measurements of ΣFe must therefore be considered separately.

---

[2]We use our own photometric data for Carina and Fornax (see Paper I). Sculptor photometry was provided by Matthew Coleman (see Coleman et al. 2005). Because of problems flat-fielding our Sextans images, for Sextans stars we list magnitudes and colors only if the stars overlap with the sample of Lee et al. (2003), and we report the Lee et al. (2003) value.
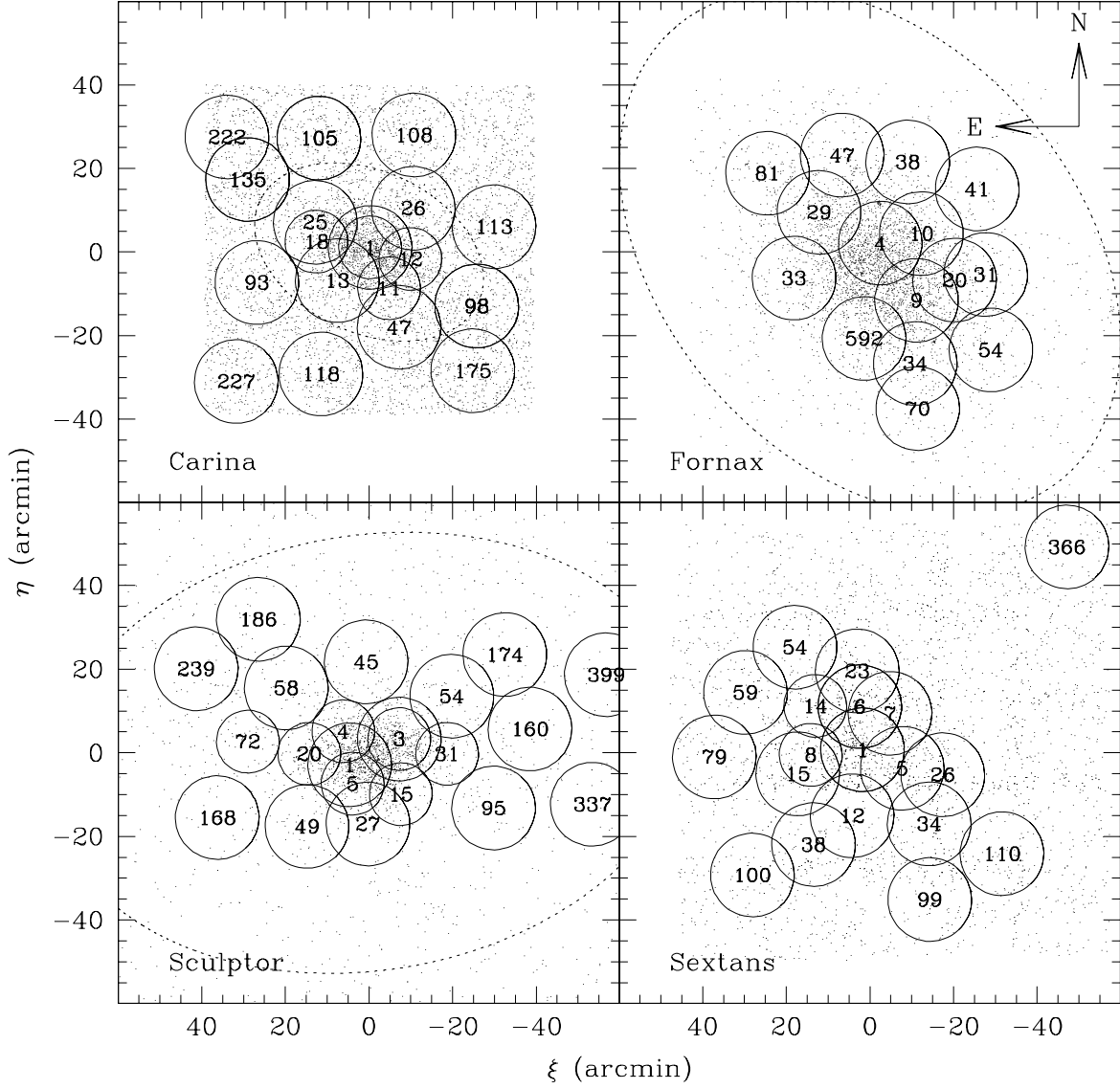
Fig. 1.— MMFS fields observed as of 2008 August. Small points represent red giant candidates as identified in Paper I. Dotted ellipses correspond to (nominal) tidal radii, as identified by King (1962) profile fits to the surface brightness profiles by Irwin & Hatzidimitriou (1995). Sextans' tidal radius ($r_t \sim 160'$) lies outside the plotted region.

Table 1.   MMFS observations of dSph fields in 2007 - 2008

| Galaxy	Field	HJD -2.45×10^6 (days)	UT Date	Exposure Time (s)	Targets	Velocities
Carina	1.1	4120.7090	2007 Jan. 20	4×2400	222	59
				1×3600	...	...
Carina	1.3	4122.7012	2007 Jan. 22	3×2400	210	121
Carina	1.4	4122.5869	2007 Jan. 22	3×2400	223	132
Sextans	1	4122.8218	2007 Jan. 22	3×2000	221	114
Carina	1.2	4123.5552	2007 Jan. 23	3×2400	218	70
Carina	98	4123.6812	2007 Jan. 23	3×2400	210	75
Sextans	59	4123.7988	2007 Jan. 23	3×2400	64	51
Carina	105	4124.6626	2007 Jan. 24	4×2400	174	70
Sextans	6	4124.8135	2007 Jan. 24	3×2400	196	109
Carina	113	4125.5474	2007 Jan. 25	4×2400	180	104
Carina	227	4125.6919	2007 Jan. 25	4×2400	124	90
Sculptor	1.1	4354.7495	2007 Sep. 11	3×2700	224	59
Fornax	4.5	4355.7222	2007 Sep. 12	3×3000	224	128
Sculptor	3.1	4357.7109	2007 Sep. 14	3×2700	218	55
Fornax	9.6	4359.6768	2007 Sep. 16	3×1800	222	96
Sculptor	3.2	4363.6250	2007 Sep. 20	5×2700	224	101
Sculptor	3.3	4364.6323	2007 Sep. 21	2×2700	218	30
				1×1900	...	...
Carina	1.2	4554.5176	2008 Mar. 29	5×2400	67	218
Carina	1.1	4557.5176	2008 Apr. 1	4×2400	102	223
				1×1800	...	...
Carina	1.5	4560.5107	2008 Apr. 3	4×2700	117	219
Sculptor	168	4683.7222	2008 Aug. 5	3×2700	25	41
Fornax	4.6	4683.8616	2008 Aug. 5	3×2400	165	222
Sculptor	174	4684.7157	2008 Aug. 6	3×2700	32	41
Fornax	47	4684.8451	2008 Aug. 6	3×2700	178	215
Sculptor	1.2	4685.7294	2008 Aug. 7	3×2400	153	205
Fornax	38	4685.8491	2008 Aug. 7	3×2700	121	143
Sculptor	399	4686.7057	2008 Aug. 8	3×2700	11	26
Fornax	41	4686.8369	2008 Aug. 8	3×2400	60	68
				1×2100	...	...
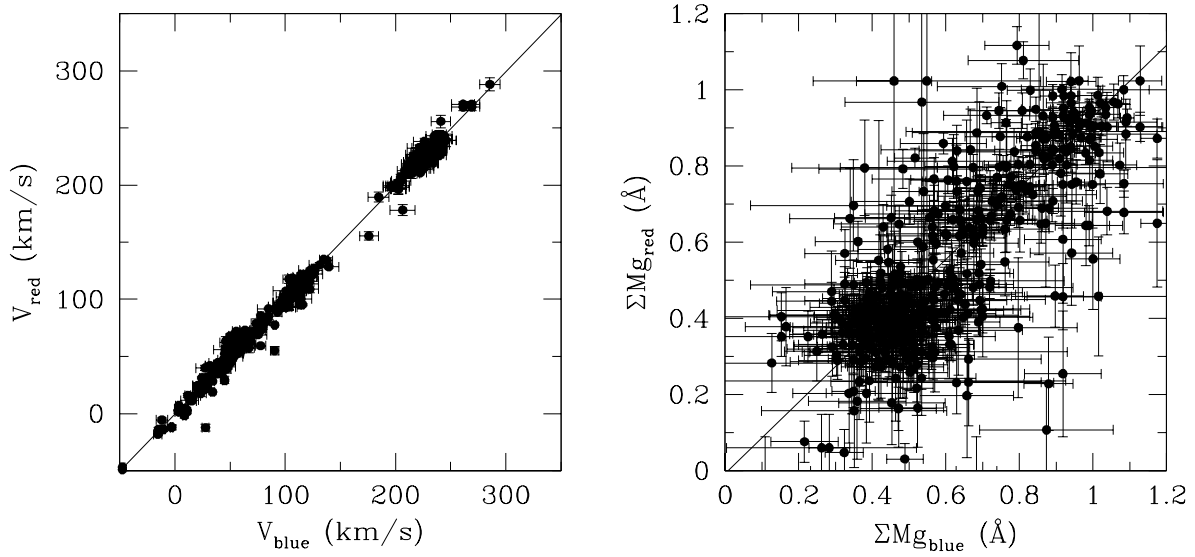
Fig. 2.— *Left:* Comparison of velocities measured for the same star on blue and red channels of the MIKE spectrograph. *Right:* Comparison of blue- and red-channel measurements of ΣMg. Overplotted in each panel is the best-fitting line.

2.1. Metallicity Calibration

In principle the ΣFe and ΣMg indices contain information about metal abundances. In order to calibrate these values onto a metallicity scale we obtained MMFS spectra of individual stars in globular clusters spanning the metallicity range $-2 \leq [\mathrm{Fe/H}] \leq -0.5$. Left-hand panels in Figure 3 plot ΣFe (top) and ΣMg (bottom) against $V - V_{HB}$, where V_{HB} is the apparent magnitude of the cluster's horizontal branch. The empirical relationship is approximately linear for each cluster, as is the case for more conventional indices derived from the calcium triplet ("CaT"; e.g., Armandroff & Da Costa 1991). The slope reflects the dependence of opacity on surface gravity and temperature, both of which correlate with $V - V_{HB}$ as an evolved star ascends the red giant branch. Following the procedure of Rutledge et al. (1997) (see also Koch et al. 2006), we assume a common slope and fit straight lines to the data from each cluster. The intercepts, known as "reduced" indices, are given by

$$\Sigma\mathrm{Fe_{blue}}' = \Sigma\mathrm{Fe_{blue}} + (0.040 \pm 0.001)(V - V_{HB}); \tag{2}$$

$$\Sigma\mathrm{Mg_{blue}}' = \Sigma\mathrm{Mg_{blue}} + (0.079 \pm 0.002)(V - V_{HB}). \tag{3}$$

and provide a measure of metal abundance that, insofar as the linear model is valid, is independent of surface gravity and temperature.

Right-hand panels in Figure 3 plot cluster metallicity, on the standard scales of Zinn & West (1984, "ZW84") and Carretta & Gratton (1997, "CG97"), against the mean reduced indices for each globular cluster. The best-fitting straight lines are given by

$$[\mathrm{Fe/H}]_{\mathrm{ZW84}} = (7.05 \pm 2.10)\Sigma\mathrm{Fe} - 3.97 \pm 2.03[2.19]; \tag{4}$$

$$[\mathrm{Fe/H}]_{\mathrm{ZW84}} = (1.93 \pm 0.16)\Sigma\mathrm{Mg}' - 2.34 \pm 0.15[0.24]; \tag{5}$$

$$[\mathrm{Fe/H}]_{\mathrm{CG97}} = (6.81 \pm 1.87)\Sigma\mathrm{Fe}' - 3.73 \pm 0.48[0.89]; \tag{6}$$

$$[\mathrm{Fe/H}]_{\mathrm{CG97}} = (1.76 \pm 0.16)\Sigma\mathrm{Mg}' - 2.11 \pm 0.10[0.20]; \tag{7}$$

where the errors include measurement errors as well as residuals from the fit, and the value in square brackets is the median metallicity error from dSph stars in the MMFS sample. The metallicities obtained from the iron indices carry large errors due to the relative weakness of the iron features in the MMFS spectra. The magnesium index thus provides our best measure of metallicity, yielding median errors of 0.20 dex on the scale of CG97 (0.24 dex on the scale of ZW84). In subsequent discussion we consider only the [Fe/H] values on the CG97 scale, obtained using Equation 7 (results are qualitatively unchanged if we use instead the values on the ZW84 scale, obtained from Equation 5).

We apply Equations 2 - 7 to obtain [Fe/H] for each dSph star in the MMFS sample. Figure 4 displays scatter plots of $[\mathrm{Fe/H}]_{\mathrm{CG97}}$ against distance from the dSph center, as well

as histograms of the global [Fe/H] distributions (results are qualitatively the same if we use the metallicity scale of ZW84). We find that the resulting metallicity distributions are significantly narrower and biased toward high metallicity with respect to distributions previously derived from CaT spectroscopy. For example, the Carina sample of Koch et al. (2006) and the Fornax sample of Battaglia et al. (2006) both contain significant numbers of stars with metallicities as low as [Fe/H]~ -2.5 dex, and as high as ~ -0.5 dex; for both galaxies the MMFS distributions fall to zero short of these extremes. While the MMFS sample ranks dSphs by mean [Fe/H] in the same sequence as previously published studies, it displays a narrower spread. These comparisons lead us to conclude that either the slope we have determined in our metallicity calibration (Equations 4 - 7) is simply too shallow, which we may remedy with observation of more calibrating clusters, or there are problems with one or both of the methods by which which Ca and Mg is used to measure iron abundance. For example, Kirby et al. (2008) have recently shown that a spectral synthesis method that fits model spectra directly to iron lines implies wider metallicity distributions than are indicated by the standard CaT method.

For analysis of the MMFS metallicity data we therefore recommend against using the absolute values of [Fe/H] that result from calibration using Equations 4 - 7. Instead we recommend using the reduced indices ΣFe and ΣMg, which are obtained by applying Equations 2 - 3 to the raw indices listed in Tables 2 - 5, as measures of *relative* metallicity. In this way the MMFS sample can be divided into metal-rich and metal-poor subcomponents, as has been done in previous analyses of these and other dSphs (e.g., Tolstoy et al. 2004; Battaglia et al. 2006), and can be used to search for evidence of metallicity gradients (Walker et al. in prep.)

2.2. Repeat Measurements

The MMFS data set contains repeat velocity measurements for 1363 dSph target stars. There are 3115 independent measurements of these stars, including up to five measurements for some stars. For subsequent analyses we replace the n_j measurements of the jth star with the weighted mean,

$$\langle V \rangle_j = \frac{\sum_{i=1}^{n_j}(w_{ij}V_{ij})}{\sum_{i=1}^{n_j} w_{ij}}, \tag{8}$$

where the weights, $w_{ij} = \sigma_{V,ij}^{-2}$, are defined by the velocity errors $\sigma_{V_{ij}}$. The weighted mean provides an unbiased estimate of the true velocity, and has variance $\sigma_{\bar{V},j}^2 = (\sum_{i=1}^{n_j} w_{ij})^{-1}$. We again use the weighted mean to combine repeat measurements (of which there are 2408 for 1089 stars) of the composite index ΣMg. For all stars with $n_j > 1$ independent velocity
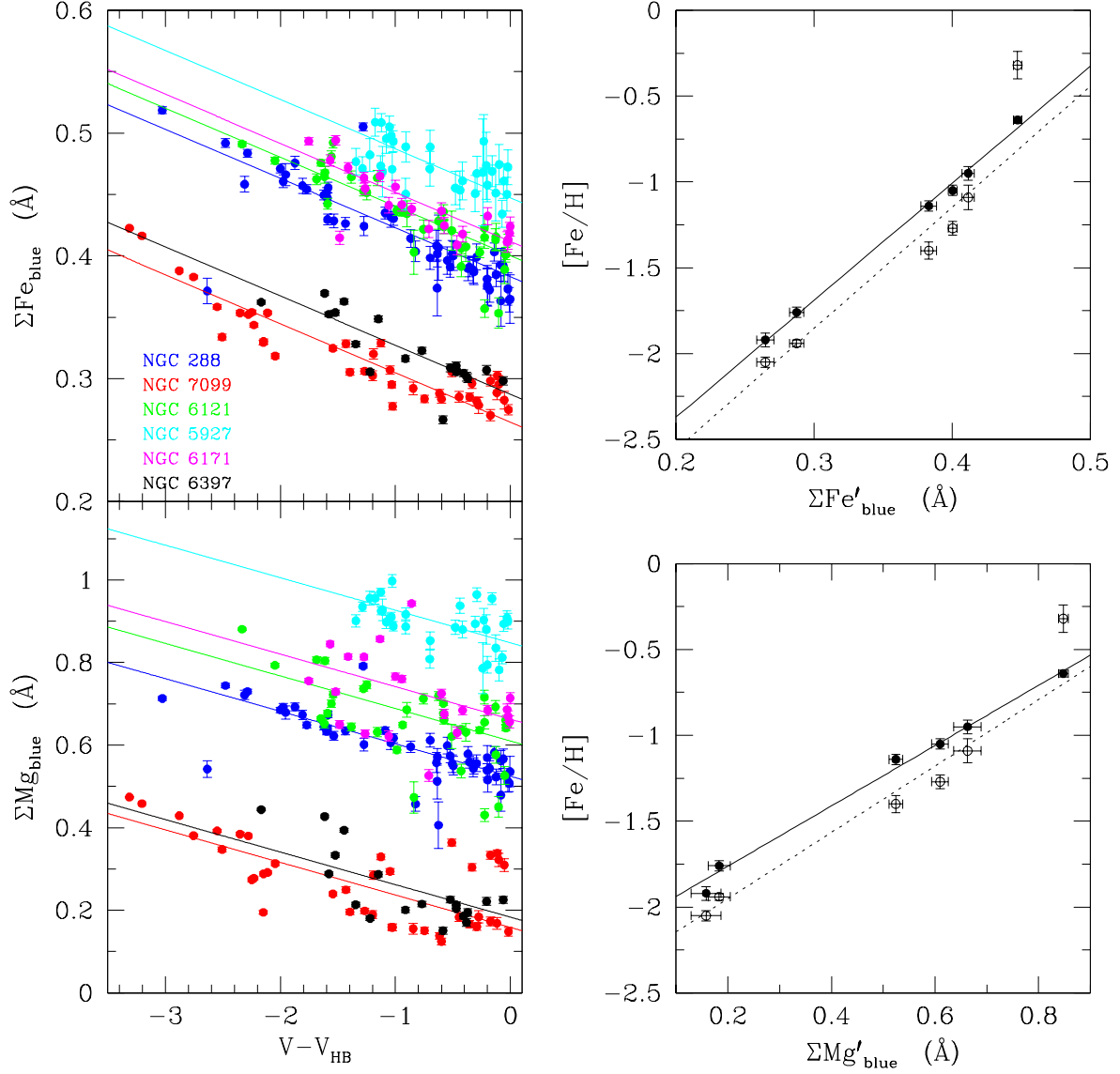
Fig. 3.— Metallicity calibration. *Left:* ΣFe (top) and ΣMg indices (bottom) versus $V - V_{HB}$ for globular cluster red giants observed with MMFS. Overplotted are lines that result from fitting a single slope as well as a unique intercept for each cluster. *Right:* Mean reduced equivalent width versus [Fe/H] for the six clusters, on the scales of Zinn & West (1984) (open circles) and Carretta & Gratton (1997) (solid circles). Overplotted for each scale is the best-fitting straight line.
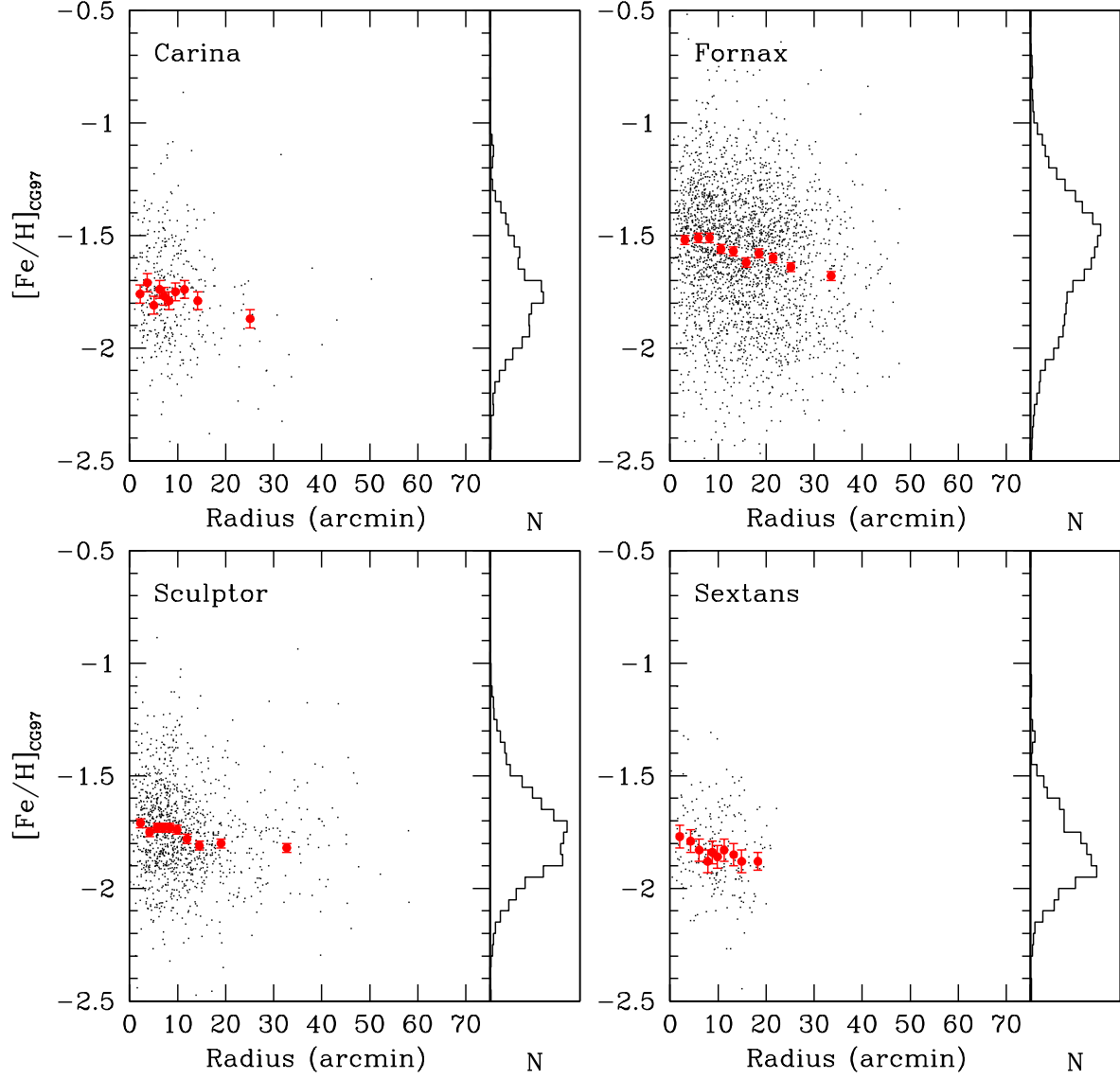
Fig. 4.— Metallicity distribution and radial dependence. Black points in each panel give the [Fe/H] metallicity measured for individual stars, calibrated on the metallicity scale of Carretta & Gratton (1997). All plotted stars are red giant candidates with membership probability $\hat{P}_{dsph} > 0.5$. Median errors for individual data points are ±0.2 dex. Red points give the mean [Fe/H] after binning the sample according to projected radius. Histograms in subpanels give the global [Fe/H] distributions.

measurements, column 12 of Tables 2 - 5 lists the weighted mean velocity. Column 13 gives the weighted mean value of ΣMg for stars with multiple measurements.

2.3. dSph Membership

We expect some fraction of the stars in each dSph sample to be contaminants—i.e., Milky Way stars with magnitudes and colors satisfying our target selection criteria. These stars tend to be either disk dwarfs or halo giants, both of which have broader velocity distributions than dSphs. Foreground dwarfs also tend to have higher metallicity and surface gravity, boosting their ΣMg values. Thus, while the dSph members cluster into relatively narrow velocity distributions, contaminants tend to have a broader velocity distribution and systematically larger ΣMg. We can therefore use the available velocity and ΣMg data to help evaluate whether a given star is a dSph member or a foreground contaminant.

In Paper III we introduce a statistical technique called expectation maximization (EM). There we develop an EM algorithm that uses the velocity and ΣMg data, as well as the positions of the observed stars, to evaluate the membership probability, P_M, of each star. These probabilities are listed in Column 11 of Tables 2-5. By adding membership probabilities, we find that there are more than 5000 probable members in the MMFS sample, including 774 Carina members, 2483 Fornax members, 1365 Sculptor members, and 441 Sextans members.

3. Summary

We have presented all spectroscopic observations of dSph stars taken with MMFS as of 2008 August. The MMFS sample more than doubles the number of velocity measurements for dSph stars, dating from Aaronson's (1983) initial kinematic study to the most recent published data from surveys using Keck and the VLT (Muñoz et al. 2006; Koch et al. 2006, 2007b,a; Battaglia et al. 2006; Battaglia et al. 2008). In forthcoming work we use the data presented here, as well as the membership probabilities, to analyze the kinematics, chemodynamics and potential substructure in these dSphs.

Table 2.   MMFS Spectroscopic Data—Carina[a]

Target	Field	HJD -2.45×10^6	α_{2000} (hh:mm:ss)	δ_{2000} (dd:mm:ss)	V (mag)	V-I (mag)	V_{helio} (km s^{-1})	ΣFe (Å)	ΣMg (Å)	$\hat{P}_M$	$\langle V \rangle_{helio}$ (km s^{-1})	$\langle \Sigma$Mg$\rangle$ (Å)
Car-0001	18B	3087.533	06:42:17.94	−50:53:58.4	19.90	1.14	218.8 ± 2.0	0.42 ± 0.05	0.48 ± 0.10	1.000	219.0 ± 2.0	0.49 ± 0.10
	1R	4554.518					223.0 ± 10.3	0.21 ± 0.28	0.53 ± 0.30			
Car-0002	18B	3087.533	06:42:18.60	−50:54:27.6	18.87	1.14	235.4 ± 0.6	0.38 ± 0.02	0.45 ± 0.05	1.000	235.5 ± 0.6	0.44 ± 0.04
	1R	3088.572					237.3 ± 5.8	0.43 ± 0.02	0.46 ± 0.09			
	25R	3411.554					236.0 ± 6.2	0.37 ± 0.07	0.24 ± 0.15			
	1R	4554.518					241.3 ± 4.0	0.43 ± 0.09	0.46 ± 0.16			
Car-0003	18B	3087.533	06:42:25.74	−50:52:12.6	18.84	1.10	39.6 ± 0.9	0.39 ± 0.04	1.12 ± 0.03	0.000		
Car-0004	18B	3087.533	06:42:27.17	−50:53:07.4	19.53	0.99	57.1 ± 1.9	0.43 ± 0.05	1.02 ± 0.06	0.000		
Car-0005	18B	3087.533	06:42:26.13	−50:53:29.1	17.99	1.35	4.6 ± 2.1	0.40 ± 0.02	0.95 ± 0.03	0.000	6.0 ± 1.8	0.95 ± 0.03
	1R	4122.587					8.8 ± 3.1	···	···			
Car-0006	18B	3087.533	06:42:27.95	−50:53:37.4	20.41	0.92	218.0 ± 3.4	···	0.87 ± 0.22	0.964		
Car-0007	18B	3087.533	06:42:25.17	−50:54:01.8	20.42	1.02	216.2 ± 5.0	0.30 ± 0.23	0.57 ± 0.25	0.997		
Car-0008	18B	3087.533	06:42:21.59	−51:00:21.4	20.47	0.84	225.1 ± 5.7	0.42 ± 0.08	0.31 ± 0.20	1.000	225.4 ± 3.1	0.24 ± 0.10
	13B	3410.547					225.6 ± 3.8	0.38 ± 0.05	0.21 ± 0.12			
Car-0009	18B	3087.533	06:42:25.55	−50:59:35.8	19.43	1.05	232.1 ± 1.9	0.42 ± 0.04	0.41 ± 0.09	1.000	232.1 ± 1.9	0.41 ± 0.09
	1R	4123.555					232.9 ± 9.2	···	···			
Car-0010	18B	3087.533	06:42:24.18	−50:56:12.6	18.48	1.20	223.2 ± 0.9	0.40 ± 0.02	0.39 ± 0.04	1.000	223.1 ± 0.8	0.39 ± 0.04
	25R	3411.554					222.5 ± 1.6	0.34 ± 0.04	0.38 ± 0.10			
Car-0011	18B	3087.533	06:42:27.59	−50:55:54.0	20.50	0.80	214.5 ± 3.4	0.37 ± 0.07	0.35 ± 0.19	1.000	217.0 ± 2.3	0.44 ± 0.09
	13B	3410.547					219.1 ± 3.2	0.35 ± 0.06	0.47 ± 0.11			
Car-0012	18B	3087.533	06:42:11.82	−50:57:13.1	19.94	1.00	229.5 ± 4.0	0.33 ± 0.05	0.39 ± 0.12	1.000		
Car-0013	18B	3087.533	06:42:16.01	−50:56:54.8	19.65	0.96	219.1 ± 1.8	0.40 ± 0.03	0.35 ± 0.09	1.000	219.3 ± 1.7	0.35 ± 0.09
	1R	4122.587					226.7 ± 11.8	···	···			
Car-0014	18B	3087.533	06:42:14.01	−50:56:58.3	20.62	0.95	232.6 ± 2.5	0.47 ± 0.07	0.42 ± 0.16	1.000		
Car-0015	18B	3087.533	06:42:14.77	−50:56:21.5	20.13	1.08	220.3 ± 2.2	0.27 ± 0.07	0.52 ± 0.12	0.999	220.5 ± 2.2	0.52 ± 0.12
	1R	4557.518					224.8 ± 11.0	···	···			
...												

[a]See electronic edition for complete data table.

Table 3.   MMFS Spectroscopic Data—Fornax[a]

Target	Field	HJD -2.45×10^6	α_{2000} (hh:mm:ss)	δ_{2000} (dd:mm:ss)	V (mag)	V-I (mag)	V_{helio} (km s^{-1})	ΣFe (Å)	ΣMg (Å)	$\hat{P}_M$	$\langle V \rangle_{helio}$ (km s^{-1})	$\langle \Sigma Mg \rangle$ (Å)
For-0001	15B	3287.826	02:39:53.25	−34:34:35.8	19.27	1.35	51.4 ± 0.4	0.51 ± 0.02	0.65 ± 0.05	0.996		
For-0002	15B	3287.826	02:39:56.10	−34:35:43.1	19.23	1.27	56.8 ± 0.5	0.51 ± 0.02	0.59 ± 0.05	0.997		
For-0003	15B	3287.826	02:39:55.28	−34:37:27.2	19.06	1.24	53.4 ± 0.4	0.50 ± 0.03	0.59 ± 0.07	0.995		
For-0004	15B	3287.826	02:39:55.69	−34:38:21.8	19.22	1.28	64.3 ± 0.6	0.56 ± 0.03	0.82 ± 0.05	0.985		
For-0005	15B	3287.826	02:39:58.47	−34:38:51.5	18.97	1.17	54.9 ± 0.5	0.49 ± 0.02	0.55 ± 0.05	0.995		
For-0006	15B	3287.826	02:39:55.36	−34:38:56.7	19.33	1.13	49.9 ± 0.8	0.49 ± 0.05	0.77 ± 0.08	0.992		
For-0007	15B	3287.826	02:39:59.50	−34:33:25.7	19.24	1.25	70.4 ± 0.5	0.57 ± 0.03	0.64 ± 0.06	0.994		
For-0008	15B	3287.826	02:40:01.52	−34:35:09.8	19.30	1.32	63.2 ± 0.5	0.62 ± 0.03	0.97 ± 0.05	0.926		
For-0009	15B	3287.826	02:40:00.13	−34:35:16.3	19.38	1.19	51.6 ± 0.5	0.54 ± 0.03	0.70 ± 0.07	0.996		
For-0010	15B	3287.826	02:39:58.41	−34:36:00.1	19.03	1.28	41.1 ± 0.4	0.53 ± 0.02	0.78 ± 0.04	0.985		
For-0011	15B	3287.826	02:40:00.18	−34:36:55.3	19.18	1.17	71.0 ± 1.6	0.49 ± 0.05	0.50 ± 0.15	0.986		
For-0012	15B	3287.826	02:40:07.09	−34:37:03.0	19.24	1.08	32.9 ± 1.2	0.35 ± 0.05	0.64 ± 0.10	0.966		
For-0013	15B	3287.826	02:40:07.35	−34:37:56.7	19.06	1.26	54.5 ± 0.6	0.58 ± 0.03	0.65 ± 0.09	0.995		
For-0014	15B	3287.826	02:40:05.29	−34:38:12.8	19.14	1.31	43.6 ± 1.0	· · ·	· · ·	0.983		
For-0015	15B	3287.826	02:40:11.40	−34:42:50.8	19.22	1.13	79.0 ± 0.8	0.43 ± 0.04	0.43 ± 0.09	0.949	79.2 ± 0.8	0.42 ± 0.08
	592B	3666.797					83.6 ± 3.2	0.38 ± 0.08	0.38 ± 0.19			
For-0016	15B	3287.826	02:40:14.65	−34:39:25.3	19.31	1.21	60.1 ± 0.8	0.47 ± 0.04	0.42 ± 0.09	0.990		
For-0017	15B	3287.826	02:40:12.08	−34:38:47.8	19.25	1.34	59.4 ± 0.5	0.45 ± 0.03	0.57 ± 0.06	0.995		
For-0018	15B	3287.826	02:40:23.40	−34:38:46.0	19.18	1.23	48.3 ± 0.7	0.43 ± 0.03	0.63 ± 0.06	0.995		
For-0019	15B	3287.826	02:40:25.26	−34:38:14.1	19.20	1.04	146.1 ± 5.7	· · ·	· · ·	0.000		
For-0020	15B	3287.826	02:40:04.61	−34:40:07.9	19.32	1.36	65.3 ± 0.6	0.50 ± 0.04	0.57 ± 0.08	0.994		
For-0021	15B	3287.826	02:39:56.33	−34:39:49.7	19.11	1.30	57.4 ± 0.7	0.50 ± 0.03	0.58 ± 0.07	0.995		
For-0022	15B	3287.826	02:40:01.03	−34:39:16.9	18.92	1.13	70.2 ± 0.7	0.44 ± 0.03	0.54 ± 0.06	0.990		
For-0023	15B	3287.826	02:40:09.10	−34:39:13.9	19.24	1.16	58.0 ± 0.6	0.50 ± 0.03	0.61 ± 0.07	0.995		
For-0024	15B	3287.826	02:40:04.67	−34:38:41.0	19.22	1.15	65.6 ± 0.6	0.54 ± 0.04	0.57 ± 0.08	0.993		
For-0025	15B	3287.826	02:40:02.44	−34:38:26.2	19.17	1.18	36.5 ± 0.6	0.51 ± 0.03	0.62 ± 0.07	0.982		
...												

[a]See electronic edition for complete data table

Table 4.   MMFS Spectroscopic Data—Sculptor[a]

Target	Field	HJD -2.45×10^6	α_{2000} (hh:mm:ss)	δ_{2000} (dd:mm:ss)	V (mag)	V-I (mag)	V_{helio} (km s^{-1})	ΣFe (Å)	ΣMg (Å)	$\hat{P}_M$	$\langle V \rangle_{helio}$ (km s^{-1})	$\langle \Sigma$Mg$\rangle$ (Å)
Scl-0001	20B	3286.629	01:00:46.17	−33:39:19.6	19.32	1.13	114.1 ± 1.9	0.36 ± 0.02	0.43 ± 0.04	0.998	112.6 ± 1.2	0.56 ± 0.03
	4B	3288.571					111.5 ± 1.6	0.34 ± 0.02	0.69 ± 0.04			
Scl-0002	20B	3286.629	01:00:45.44	−33:39:59.9	18.72	1.15	110.1 ± 0.9	0.32 ± 0.01	0.39 ± 0.03	1.000	110.2 ± 0.9	0.40 ± 0.03
	4R	3288.571					111.5 ± 2.6	0.27 ± 0.03	0.42 ± 0.08			
Scl-0003	20B	3286.629	01:00:44.46	−33:41:54.1	19.91	1.14	118.4 ± 2.8	0.42 ± 0.04	0.53 ± 0.06	1.000	116.4 ± 1.9	0.50 ± 0.05
	1B	4017.555					114.8 ± 2.5	0.32 ± 0.05	0.39 ± 0.11			
Scl-0004	20B	3286.629	01:00:46.96	−33:43:19.9	19.47	1.15	95.6 ± 2.2	0.38 ± 0.02	0.34 ± 0.05	1.000	103.8 ± 0.7	0.34 ± 0.03
	4B	3288.571					104.5 ± 2.0	0.30 ± 0.02	0.32 ± 0.05			
	1B	4017.555					104.6 ± 0.8	0.36 ± 0.03	0.36 ± 0.07			
Scl-0005	20B	3286.629	01:00:42.44	−33:43:26.0	19.11	1.18	115.5 ± 2.1	0.43 ± 0.02	0.33 ± 0.04	1.000	117.7 ± 0.9	0.40 ± 0.03
	4R	3288.571					115.5 ± 7.9	0.39 ± 0.04	0.52 ± 0.10			
	5R	3289.593					114.6 ± 3.3	0.40 ± 0.03	0.53 ± 0.09			
	1B	4017.555					118.7 ± 1.1	0.38 ± 0.04	0.50 ± 0.08			
Scl-0006	20B	3286.629	01:00:44.88	−33:43:57.7	19.17	1.11	93.0 ± 2.3	0.38 ± 0.02	0.31 ± 0.05	0.999	93.4 ± 2.2	0.32 ± 0.05
	4R	3288.571					100.7 ± 10.1	0.15 ± 0.08	0.37 ± 0.14			
Scl-0007	20B	3286.629	01:00:42.07	−33:44:02.7	19.26	1.18	118.6 ± 2.0	0.29 ± 0.04	0.63 ± 0.05	0.991		
Scl-0008	20B	3286.629	01:00:51.01	−33:38:20.5	18.97	1.13	113.8 ± 4.9	0.30 ± 0.02	0.63 ± 0.03	0.984	103.6 ± 1.4	0.60 ± 0.03
	1B	4017.555					102.7 ± 1.5	0.33 ± 0.04	0.39 ± 0.08			
Scl-0009	20B	3286.629	01:00:50.99	−33:40:02.4	18.50	1.17	95.7 ± 0.8	0.39 ± 0.01	0.42 ± 0.03	0.999	95.7 ± 0.8	0.41 ± 0.03
	4R	3288.571					97.0 ± 4.1	0.33 ± 0.03	0.32 ± 0.09			
Scl-0010	20B	3286.629	01:00:49.48	−33:40:37.8	18.98	1.16	101.6 ± 1.6	0.33 ± 0.02	0.39 ± 0.03	1.000	101.6 ± 1.6	0.41 ± 0.03
	4R	3288.571					101.9 ± 5.1	0.40 ± 0.03	0.59 ± 0.09			
Scl-0011	20B	3286.629	01:00:51.15	−33:47:17.3	19.39	1.04	112.6 ± 4.8	0.34 ± 0.03	0.51 ± 0.05	1.000	114.9 ± 1.1	0.49 ± 0.04
	1B	4017.555					115.0 ± 1.1	0.37 ± 0.04	0.43 ± 0.09			
Scl-0012	20B	3286.629	01:00:51.95	−33:46:24.0	19.12	1.20	111.8 ± 0.8	0.36 ± 0.02	0.46 ± 0.04	1.000	111.3 ± 0.4	0.45 ± 0.03
	5R	3289.593					112.4 ± 11.2	0.30 ± 0.04	0.48 ± 0.10			
	1B	4017.555					111.0 ± 0.5	0.39 ± 0.03	0.39 ± 0.06			
...												

[a]See electronic edition for complete data table.

Table 5.   MMFS Spectroscopic Data—Sextans[a]

Target	Field	HJD -2.45×10^6	α_{2000} (hh:mm:ss)	δ_{2000} (dd:mm:ss)	V (mag)	V-I (mag)	V_{helio} (km s^{-1})	ΣFe (Å)	ΣMg (Å)	$\hat{P}_M$	$\langle V \rangle_{helio}$ (km s^{-1})	$\langle \Sigma$Mg$\rangle$ (Å)
Sex-0001	8B	3086.796	10:14:25.29	−01:42:53.7	19.70	0.62	269.4 ± 2.5	0.35 ± 0.03	0.45 ± 0.07	0.000	270.2 ± 1.7	0.32 ± 0.06
	15B	3417.761					270.9 ± 2.2	0.31 ± 0.03	0.14 ± 0.09			
Sex-0002	8B	3086.796	10:14:31.87	−01:39:06.6	$\cdots$	$\cdots$	47.3 ± 2.5	0.36 ± 0.02	0.99 ± 0.03	0.000	47.1 ± 1.4	0.92 ± 0.02
	15B	3417.761					47.1 ± 1.8	0.35 ± 0.02	0.84 ± 0.03			
Sex-0003	8B	3086.796	10:14:27.43	−01:37:24.8	$\cdots$	$\cdots$	123.8 ± 3.2	0.28 ± 0.03	1.05 ± 0.04	0.000	123.3 ± 2.0	0.92 ± 0.03
	15B	3417.761					122.9 ± 2.6	0.34 ± 0.02	0.80 ± 0.04			
Sex-0004	8B	3086.796	10:14:18.28	−01:44:08.4	18.49	1.33	29.8 ± 2.5	0.30 ± 0.05	1.00 ± 0.06	0.000	30.1 ± 1.8	0.85 ± 0.03
	15B	3417.761					30.4 ± 2.5	0.33 ± 0.02	0.80 ± 0.04			
Sex-0005	8B	3086.796	10:14:18.50	−01:39:59.3	18.06	1.25	31.9 ± 1.9	0.38 ± 0.02	0.98 ± 0.02	0.000	32.4 ± 1.3	0.94 ± 0.01
	15B	3417.761					32.8 ± 1.8	0.37 ± 0.01	0.89 ± 0.02			
Sex-0006	8B	3086.796	10:14:20.25	−01:39:23.0	19.77	0.73	273.5 ± 4.0	0.28 ± 0.05	0.48 ± 0.12	0.000	271.6 ± 1.8	0.62 ± 0.05
	15B	3417.761					271.1 ± 2.1	0.35 ± 0.03	0.64 ± 0.05			
Sex-0007	8B	3086.796	10:14:17.73	−01:38:28.7	19.42	0.58	147.6 ± 3.0	0.24 ± 0.04	0.48 ± 0.08	0.000	145.9 ± 2.0	0.37 ± 0.05
	15B	3417.761					144.5 ± 2.8	0.25 ± 0.03	0.30 ± 0.06			
Sex-0008	8B	3086.796	10:14:06.42	−01:34:50.0	17.55	1.26	-9.0 ± 1.7	0.35 ± 0.01	0.87 ± 0.02	0.000		
Sex-0009	8B	3086.796	10:14:08.40	−01:35:49.1	19.52	0.90	223.6 ± 4.9	0.31 ± 0.03	0.35 ± 0.07	0.998	226.1 ± 1.7	0.31 ± 0.05
	15B	3417.761					226.4 ± 1.8	0.26 ± 0.03	0.28 ± 0.06			
Sex-0010	8B	3086.796	10:14:17.31	−01:35:55.0	$\cdots$	$\cdots$	-39.6 ± 2.6	0.35 ± 0.02	0.77 ± 0.04	0.000	-39.8 ± 1.6	0.81 ± 0.02
	15B	3417.761					-40.0 ± 2.1	0.37 ± 0.02	0.84 ± 0.03			
Sex-0011	8B	3086.796	10:14:15.20	−01:36:16.9	19.77	1.02	72.8 ± 3.0	0.31 ± 0.04	0.93 ± 0.06	0.000	64.6 ± 0.8	0.84 ± 0.04
	15B	3417.761					64.0 ± 0.8	0.37 ± 0.04	0.73 ± 0.07			
Sex-0012	8B	3086.796	10:14:21.75	−01:31:45.0	18.12	0.82	317.0 ± 1.5	0.33 ± 0.01	0.59 ± 0.02	0.000		
Sex-0013	8B	3086.796	10:14:16.38	−01:44:00.5	20.36	1.20	110.9 ± 3.5	0.43 ± 0.06	0.56 ± 0.13	0.000		
Sex-0014	8B	3086.796	10:14:01.64	−01:45:32.9	18.77	1.17	16.9 ± 1.8	0.41 ± 0.03	0.81 ± 0.04	0.000	16.8 ± 1.4	0.80 ± 0.03
	15B	3417.761					16.5 ± 2.1	0.36 ± 0.03	0.79 ± 0.04			
Sex-0015	8B	3086.796	10:13:55.24	−01:33:20.5	19.80	0.95	246.2 ± 4.4	0.34 ± 0.04	0.38 ± 0.09	0.997	223.9 ± 1.4	0.40 ± 0.06
	7B	3090.704					233.6 ± 5.1	0.30 ± 0.10	0.07 ± 0.25			
	15B	3417.761					220.2 ± 1.6	0.34 ± 0.04	0.44 ± 0.07			
...												

[a]See electronic edition for complete data table.

REFERENCES

Aaronson, M. 1983, ApJ, 266, L11

Aaronson, M., & Olszewski, E. W. 1987, AJ, 94, 657

Armandroff, T. E., & Da Costa, G. S. 1991, AJ, 101, 1329

Armandroff, T. E., Olszewski, E. W., & Pryor, C. 1995, AJ, 110, 2131

Battaglia, G., Helmi, A., Tolstoy, E., Irwin, M., Hill, V., & Jablonka, P. 2008, astro-ph/0802.4220, 802

Battaglia et al. 2006, A&A, 459, 423

Bernstein, R., Shectman, S. A., Gunnels, S. M., Mochnacki, S., & Athey, A. E. 2003, in Instrument Design and Performance for Optical/Infrared Ground-based Telescopes. Edited by Iye, Masanori; Moorwood, Alan F. M. Proceedings of the SPIE, Volume 4841, pp. 1694-1704 (2003)., ed. M. Iye & A. F. M. Moorwood, 1694–1704

Carretta, E., & Gratton, R. G. 1997, A&AS, 121, 95

Coleman, M. G., Da Costa, G. S., & Bland-Hawthorn, J. 2005, AJ, 130, 1065

Gilmore, G., Wilkinson, M. I., Wyse, R. F. G., Kleyna, J. T., Koch, A., & Wyn Evans, N. 2007, astro-ph/0703308

Hargreaves, J. C., Gilmore, G., & Annan, J. D. 1996, MNRAS, 279, 108

Hargreaves, J. C., Gilmore, G., Irwin, M. J., & Carter, D. 1994, MNRAS, 271, 693

Irwin, M., & Hatzidimitriou, D. 1995, MNRAS, 277, 1354

King, I. 1962, AJ, 67, 471

Kirby, E. N., Simon, J. D., Geha, M., Guhathakurta, P., & Frebel, A. 2008, ApJ, 685, L43

Kleyna, J., Wilkinson, M. I., Evans, N. W., Gilmore, G., & Frayn, C. 2002, MNRAS, 330, 792

Kleyna, J. T., Wilkinson, M. I., Evans, N. W., & Gilmore, G. 2004, MNRAS, 354, L66

Kleyna, J. T., Wilkinson, M. I., Gilmore, G., & Evans, N. W. 2003, ApJ, 588, L21

Koch, A., Grebel, E. K., Wyse, R. F. G., Kleyna, J. T., Wilkinson, M. I., Harbeck, D. R., Gilmore, G. F., & Evans, N. W. 2006, AJ, 131, 895

Koch, A., Kleyna, J. T., Wilkinson, M. I., Grebel, E. K., Gilmore, G. F., Evans, N. W., Wyse, R. F. G., & Harbeck, D. R. 2007a, AJ, 134, 566

Koch, A., Wilkinson, M. I., Kleyna, J. T., Gilmore, G. F., Grebel, E. K., Mackey, A. D., Evans, N. W., & Wyse, R. F. G. 2007b, ApJ, 657, 241

Lee, M. G., Park, H. S., Park, J.-H., Sohn, Y.-J., Oh, S. J., Yuk, I.-S., Rey, S.-C., Lee, S.-G., Lee, Y.-W., Kim, H.-I., Han, W., Park, W.-K., Lee, J. H., Jeon, Y.-B., & Kim, S. C. 2003, AJ, 126, 2840

Łokas, E. L., Mamon, G. A., & Prada, F. 2005, MNRAS, 363, 918

Mateo, M., Olszewski, E., Welch, D. L., Fischer, P., & Kunkel, W. 1991, AJ, 102, 914

Mateo, M., Olszewski, E. W., Pryor, C., Welch, D. L., & Fischer, P. 1993, AJ, 105, 510

Mateo, M., Olszewski, E. W., Vogt, S. S., & Keane, M. J. 1998, AJ, 116, 2315

Mateo, M., Olszewski, E. W., & Walker, M. G. 2008, ApJ, 675, 201

Muñoz et al. 2005, ApJ, 631, L137

—. 2006, ApJ, 649, 201

Olszewski, E. W., Aaronson, M., & Hill, J. M. 1995, AJ, 110, 2120

Queloz, D., Dubath, P., & Pasquini, L. 1995, A&A, 300, 31

Rutledge, G. A., Hesser, J. E., & Stetson, P. B. 1997, PASP, 109, 907

Sohn et al. 2007, ApJ, 663, 960

Strigari, L. E., Bullock, J. S., Kaplinghat, M., Simon, J. D., Geha, M., Willman, B., & Walker, M. G. 2008, Nature, 454, 1096

Suntzeff, N. B., Mateo, M., Terndrup, D. M., Olszewski, E. W., Geisler, D., & Weller, W. 1993, ApJ, 418, 208

Tolstoy et al. 2004, ApJ, 617, L119

Vogt, S. S., Mateo, M., Olszewski, E. W., & Keane, M. J. 1995, AJ, 109, 151

Walker, M. G., Mateo, M., Olszewski, E. W., Bernstein, R., Sen, B., & Woodroofe, M. 2007a, ApJS, 171, 389

Walker, M. G., Mateo, M., Olszewski, E. W., Bernstein, R., Wang, X., & Woodroofe, M. 2006a, AJ, 131, 2114

Walker, M. G., Mateo, M., Olszewski, E. W., Gnedin, O. Y., Wang, X., Sen, B., & Woodroofe, M. 2007b, ApJ, 667, L53

Walker, M. G., Mateo, M., Olszewski, E. W., Pal, J. K., Sen, B., & Woodroofe, M. 2006b, ApJ, 642, L41

Walker, M. G., Mateo, M., Olszewski, E. W., Sen, B., & Woodroofe, M. 2008, in prep. (Paper III)

Wilkinson, M. I., Kleyna, J. T., Evans, N. W., Gilmore, G. F., Irwin, M. J., & Grebel, E. K. 2004, ApJ, 611, L21

Zinn, R., & West, M. J. 1984, ApJS, 55, 45